Characterization of Random Telegraph Signal in Neutron-Irradiated 150-nm CMOS SPADs

F. Shojaei, P. Brogi, G.-F. Dalla Betta, *Senior Member, IEEE*, V. Goiffon, *Senior Member, IEEE*, P. S. Marrocchesi, J. Minga, L. Pancheri, *Senior Member, IEEE*, G. Torilla, L. Ratti, *Senior Member, IEEE*, and C. Vacchi

***Abstract*—This article investigates the neutron irradiation effects on the random telegraph signal (RTS) observed in the dark count rate (DCR) of single-photon avalanche diodes (SPADs) fabricated in a 150-nm complementary metal–oxide–semiconductor (CMOS) technology. Two similar chips, F2 and S2, were exposed to neutron fluences of 4.15×10^{10} and 3.90×10^{9} 1 MeV neutron equivalent cm^{-2}, respectively. Time-resolved DCR measurements were acquired both before and after irradiation. RTS detection and characterization techniques are discussed, revealing that although the weighted-time-lag plot (W-TLP) is effective in accurately detecting RTS levels, it presents challenges in extracting other RTS characteristics. The primary effect observed in the irradiated samples is an increase in the number of pixels exhibiting RTS post-irradiation, along with more complex RTS behavior, attributed to multi-stable RTS defects in neutron-induced clusters. To further understand these defects, temperature- and voltage-dependent measurements were conducted.**

***Index Terms*—Complementary metal–oxide–semiconductor (CMOS), dark count rate (DCR), random telegraph signal (RTS), single photon avalanche diodes (SPADs).**

I. Introduction

SINGLE photon avalanche diodes (SPADs) are reverse biased p-n junctions featuring remarkable sensitivity and timing resolution, thanks to their internal high gain. The introduction of complementary metal–oxide–semiconductor (CMOS) technology in SPAD manufacturing makes it feasible to integrate front-end circuits with the detecting element, thereby enhancing data processing speed and reducing costs. These advantages make CMOS SPADs highly sought after for a wide range of applications, including time of flight (TOF) light detection and ranging (LIDAR) [1] and positron emission tomography [2], to mention just a few.

Despite these advantages, CMOS SPADs may be prevented from working effectively by random generation of avalanche pulses, which may take place even in the absence of light. This phenomenon is characterized by means of the dark count rate (DCR), which is indeed the frequency of random pulses occurring per second under dark conditions. DCR can be attributed to defects within the active region of the SPADs, incurred during the fabrication process or induced by subsequent irradiation. These defects introduce energy levels inside the silicon bandgap and contribute to the random generation of signals, with several thermal and tunneling mechanisms at play [3]. Additionally, the lattice defects inside the active volume may be responsible for the so-called random telegraph signal (RTS) noise, manifesting as fluctuations in the DCR between two or more discrete levels [4], [5]. This feature makes the calibration procedure difficult in SPAD-based detection systems, possibly degrading their reliability [5], [6]. In certain applications, such as in high-energy physics, astrophysics experiments, and in radio-diagnostic medical equipment [7], SPADs are required to withstand some level of radiation. Numerous studies on SPAD arrays subjected to irradiation, predominantly with protons [8], [9], [10] and with gamma rays [11], have demonstrated that such exposure can increase the number of pixels exhibiting RTS behavior. This phenomenon stems from displacement damage that creates vacancies and interstitials within the lattice. Such defects can then migrate, coalescing into more stable entities, such as divacancies or multivacancies, or phosphorus–vacancy (P–V) centers [12]. The formation of these complexes can induce fluctuations in the DCR. Mechanisms like inter-center charge transfer in divacancies or multivacancies or dipole moment reorientation in P–V centers [10] have been proposed to explain RTS fluctuations. However, for the time being, there is no compelling experimental evidence supporting such mechanisms as the origin of RTS. An alternative and more robust hypothesis for the origin of RTS posits the existence of defects possessing multi-stable configurations that depend on their charge state. As confirmed by simulations in [13], a large number of defects within a cluster may form a basin — a confined region containing several potential wells separated by small energy barriers. The entire basin is enclosed by a significantly higher energy barrier. Each potential well within the basin corresponds to

Received 12 September 2025; accepted 21 October 2025. Date of publication 4 November 2025; date of current version 18 December 2025. This work was supported by the ASAP Project through the Italian Institute for Nuclear Physics (INFN). *(Corresponding author: F. Shojaei.)*

F. Shojaei, G. Torilla, L. Ratti, and C. Vacchi are with Dipartimento di Ingegneria Industriale e dell'Informazione, Università degli Studi di Pavia, 27100 Pavia, Italy, and also with INFN Pavia, 27100 Pavia, Italy (e-mail: fatemeh.shojaei01@universitadipavia.it; lodovico.ratti@unipv.it).

P. Brogi and P. S. Marrocchesi are with DFSTA, Università di Siena, 53100 Siena, Italy, and also with INFN Pisa, 56127 Pisa, Italy.

G.-F. Dalla Betta and L. Pancheri are with Dipartimento di Ingegneria Industriale, Università di Trento, 38122 Trento, Italy, and also with INFN TIFPA, 38123 Trento, Italy.

V. Goiffon is with ISAE-SUPAERO, Università de Toulouse, 31055 Toulouse, France.

J. Minga is with the Albanian University, 1001 Tirana, Albania.

Color versions of one or more figures in this article are available at https://doi.org/10.1109/TNS.2025.3629317.

Digital Object Identifier 10.1109/TNS.2025.3629317

a distinct configuration, and despite the small energy barriers between them, the associated lifetimes are long enough for these configurations to be experimentally detectable [13]. Each configuration corresponds to an energy level in the Si bandgap, thereby resulting in a distinct DCR level [14]. An example of this is a divacancy, for which three associated energy levels ($E_c - 0.23$, $E_c - 0.41$, and $E_v + 0.21$) in the bandgap have been identified, with the one closest to midgap exhibiting the highest generation rate [15].

RTS noise is primarily characterized by the amplitude of transitions among distinct DCR levels, as well as by the associated level and transition time constants. The level time constant represents the average time the DCR spends at a specific level of an RTS fluctuation, regardless of the subsequent transition, while the transition time constant reflects the average time before a particular transition occurs, that is, the average interval between two consecutive transitions of the same kind (i.e., between the same two levels) [16]. These parameters, known to vary with temperature and voltage, may serve as tools to determine the characteristics of the defect causing RTS generation. For instance, in bi-level RTS observed in MOSFET devices, caused by the trapping and detrapping of channel electrons by border traps, analyzing how the ratio of high to low-level time constants changes with temperature can reveal the energy of the trap within the bandgap [17].

In this article, the RTS characteristics of CMOS SPAD arrays, fabricated using a 150-nm CMOS technology, are investigated both before and after neutron irradiation. As in the case of proton irradiation, it is observed that neutron irradiation can lead to an increase in the number of pixels displaying RTS behavior. Section II provides a detailed overview of the chip architecture and the setup used for RTS measurements. Section III elaborates on the two automated methods currently established in the literature for the comprehensive characterization of RTS noise. A key distinction between these methods lies in their RTS transition detection criteria, which affect the accuracy and reliability of RTS event identification. In the same section, additional RTS investigation tools, such as the weighted time lag plot (W-TLP) analysis, will also be discussed. Section IV is dedicated to the presentation and analysis of the experimental results, setting the stage for the concluding remarks.

II. Materials and Methods

A. Device and Neutron Source Description

In this article, the RTS observed in the DCR of CMOS SPADs, manufactured using a commercial 150-nm CMOS technology, was analyzed both before and after exposure to neutron irradiation. The study focuses on two chips, labeled as F2 and S2, each with a thickness of 150 μm. F2 was exposed to a fluence of 4.15×10^{10} 1 MeV neutron equivalent cm^{-2} (1 MeV neq cm^{-2} henceforth), while S2 was subjected to a fluence of 3.90×10^9 1 MeV neq cm^{-2}. Detailed descriptions of the 1 MeV neq cm^{-2} fluence calculation and the corresponding NIEL values are provided in [18]. Neutrons are produced by bombarding a beryllium (Be) target with 5-MeV protons. The resulting neutron energy spectrum spans from 0.5 MeV to nearly 3.5 MeV, with a prominent peak around 0.5 MeV and a smaller one near 2.5 MeV [19]. The two chips are identical except for a minor difference in their readout electronics and their dimensions, which are 5.4 × 5 mm for S2 and 6×5 mm for F2. These minor differences are associated with the implementation of a dual-layer SPAD array detector, a feature beyond the scope of this article and elaborated further in [20]. Each chip contains, among other structures, two arrays of SPADs, designated as A1 and A3, with their characteristics detailed in Table I.

TABLE I
Array A1 and A3 Characteristics

array	no. of pixels	pixel pitch (μm)	fill factor	active area (μm^2)
$A1$	2304	75	66%	70×52
$A3$	1728	50	39%	44×24

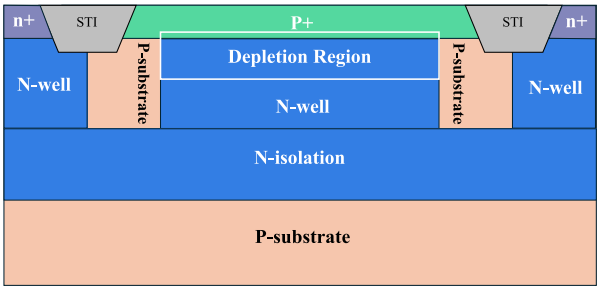

Fig. 1. Simplified cross section of the SPAD device employed in arrays A1 and A3.

The avalanche is suppressed in both arrays by passive quenching circuitry. A cross-sectional view of the detector structure, identical for all pixels within the two arrays, is illustrated in Fig. 1. The SPAD structure consists of a p+/n-well junction with an active region about 1-μm thick, encircled by a weakly doped p-substrate serving as a guard ring to prevent premature-edge breakdown [21]. The average breakdown voltage measured at room temperature for arrays A1 and A3 in F2 is approximately 16.70 V, whereas for arrays in S2, it is about 18.75 V. No significant change was detected in these values following irradiation. A more thorough description of the chips and readout electronics can be found in [20].

B. RTS Measurement Setup

For DCR measurements, the entire A1 and A3 arrays are scanned. To accelerate the process, nine SPADs at a time (6 from array A1 and 3 from array A3) are activated and read out simultaneously for a duration Δt. The activation time is set to $\Delta t = 10\ \mu$ s for measurements performed before irradiation and 1 μs for measurements conducted after irradiation. The reduction in Δt after irradiation is intended to prevent saturation and to increase the maximum measurable DCR. After each activation time, SPADs are reset and then activated again, up to a total integration time (TIT)

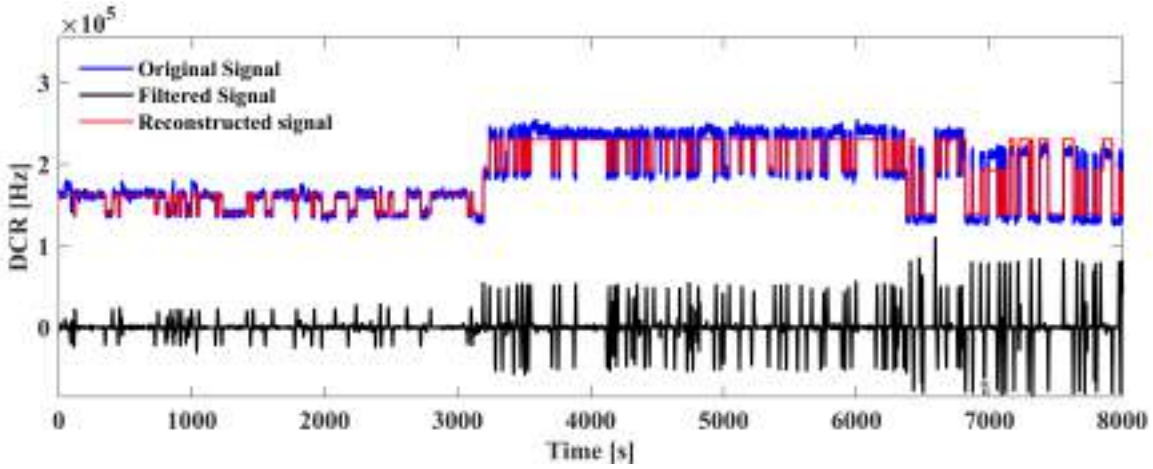

Fig. 2. Time-resolved DCR of pixel 14×45 chosen from F2/A1 at an excess voltage V_{ex} = 2 V and temperature of −10 °C after irradiation. The reconstructed signal is depicted by the red line superimposed on the originally recorded signal. The black line shows the filtered signal.

of 100 ms for measurements performed before irradiation, 20 ms for measurements carried out afterward. To accurately determine the time constants associated with RTS, long time-resolved DCR measurements are required [17]. The RTS measurements in this study can be categorized into two types: high-resolution (sampling interval = 1 Hz, i.e., once per second) and low-resolution (sampling interval = 0.016 Hz, i.e., once per minute). The term *sampling interval* refers to the time between two consecutive DCR measurements and should not be confused with DCR frequency itself. Although the DCR is measured within TIT of 100 or 20 ms, the sampling interval is limited because, after each activation window Δt, the one-bit latch memory at the output must be read, reset, and the selected pixels re-enabled before the next activation window, with additional overhead for data transfer at the end of each TIT. Measurements at low-resolution were conducted over approximately four days on all SPADs in arrays A1 and A3, which were biased at an excess voltage V_{ex} = 1.5 V and maintained at a temperature of 25 °C, both before and following neutron irradiation. Conversely, high-resolution measurements are exclusively performed on a selected subset of SPADs that have been identified as pixels showing RTS behavior (RTS pixels) from the first set of low-resolution measurements.

Furthermore, in the case of high-resolution measurements, time-resolved DCR is acquired in a DY110C ACS climatic chamber at temperatures between −20 °C and 50 °C, with increments of 10 °C, to study the temperature dependency of DCR and RTS. These measurements were performed at three different excess voltages, 1, 1.5, and 2 V, before irradiation and at two excess voltages, 1 and 2 V, after irradiation.

III. RTS Characterization Algorithms

A. RTS Detection Algorithm

For automated RTS characterization, an analysis tool based on the edge detection method, introduced in [16], was used. The tool, developed in MATLAB, operates as follows: initially, the signal is processed through a step-shaped filter with L coefficients. Consider the time-resolved DCR of pixel 14×45 from F2/A1, showing a four-level RTS as illustrated in Fig. 2. The filtering reduces Poisson noise and highlights RTS transitions, as demonstrated by the filtered signal in the same figure.

To determine the number of levels and their corresponding values, the transition time indices within the filtered signal are identified and used to divide the original signal into segments between adjacent transitions. For every segment i, the DCR mean and standard deviation are calculated and stored in $M_{seg}(i)$ and $\sigma_{seg}(i)$, respectively. After rearranging the vector M_{seg} in ascending order, each time $M_{seg}(i)$ is higher than the detected levels by at least σ_{noise} (which is obtained by averaging over σ_{seg}) or more, a new level is detected whose value is considered to be $M_{seg}(i)$.

To extract the time constants, the signal was first reconstructed by associating each segment with one of the identified levels, based on its mean DCR. The reconstructed signal is then generated using the stairs function in MATLAB, which maps each interval between two consecutive transition indices to the corresponding segment level. The reconstructed signal is depicted in red in Fig. 2. After reconstruction, the distributions of the time spent at each detected level were obtained and used to determine the magnitude and transition time constants for each level.

B. Detection Method Based on Real-Time Noise

To reduce detection failures of low-amplitude RTS in multilevel RTS traces, it is recommended in [22] to use real-time noise as the RTS detection threshold. Different from the previously described edge detection method, which considers a transition as an RTS transition if its amplitude exceeds the signal standard deviation σ_{sig}, this technique instead compares the amplitude of the candidate transition, $\text{Amp}(i+1)$, to the standard deviation of the previous segment, $\sigma_{seg}(i)$, representing the real-time noise. This enables the detection of low-amplitude RTS transitions that would otherwise go unnoticed. All detection steps after this point remain the same as in the previous algorithm. A key point here is to

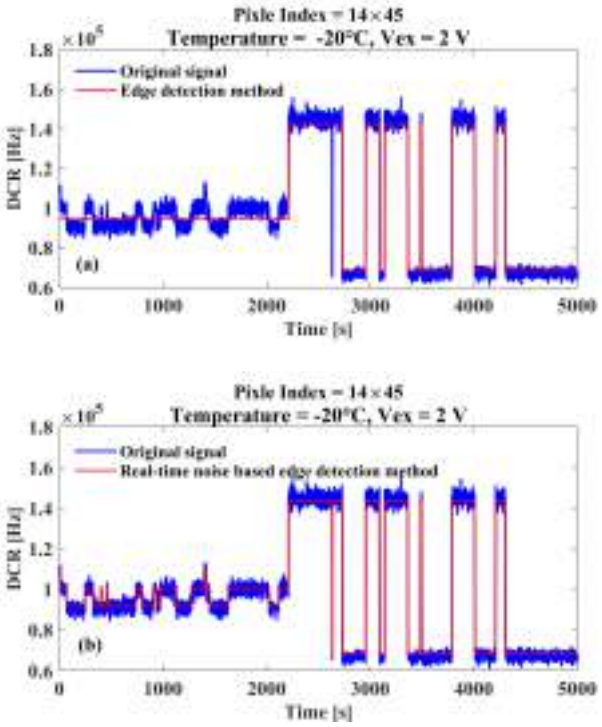

Fig. 3. Constrained DCR trace of a pixel in F2/A1 after irradiation, overlaid with reconstructed signals (a) using the edge detection method and (b) using the real-time noise based edge detection method.

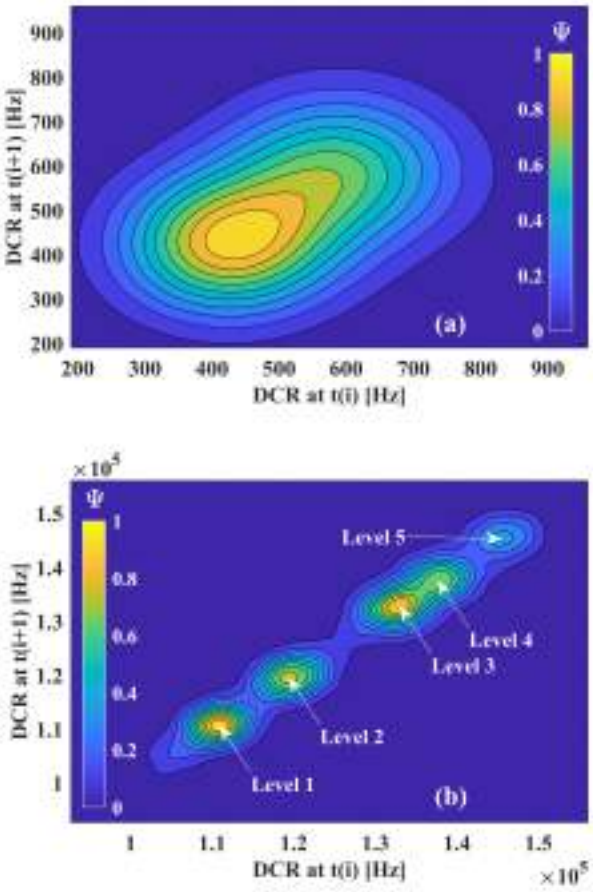

Fig. 4. W-TLP of pixel 11 × 22 from F2/A1 at an excess voltage V_{ex} = 2 V and −20 °C temperature (a) before irradiation and (b) after a fluence of 4.3×10^{10} 1 MeV neq cm^{-2}.

define candidate transitions accurately, because considering very small transitions as RTS ones may lead to classifying as RTS what is actually a simple Poisson fluctuation and to underestimating the noise standard deviation. The appropriate threshold for considering transitions as candidates in this study was assumed as $0.5 \times \sigma_{sig}$ for pre-irradiation signals and $0.2 \times \sigma_{sig}$ for post-irradiation signals. Fig. 3(a) and (b) presents signal traces from a pixel in F2/A1 after irradiation, along with the corresponding reconstructed signals. The plot in Fig. 3(a) illustrates the reconstructed signal using the edge detection method, while the one in Fig. 3(b) shows the result of a real-time noise based edge detection approach. Using the former method, smaller RTS transitions with amplitudes below the threshold of $2/\sqrt{3} \times \sigma_{noise}$ are not detected [16]. In contrast, the real-time noise-based method is capable of identifying them.

C. Weighted Time Lag Method

In certain multilevel RTS pixels, particularly when background noise is significantly high, accurately detecting levels becomes challenging, even with the aid of a time lag plot, which is constructed by plotting the DCR at time index (i), $t(i)$, on the x-axis against the DCR at $t(i+1)$ on the y-axis. Through this method, RTS levels can be detected as significantly populated regions along the diagonal [23].

However, the conventional time lag plot struggles with the extraction of useful data due to the interference caused by overlapping background noise. A solution to this issue is the adoption of a W-TLP. This plot is derived by calculating the probability of occurrence for each point in the time lag plot, followed by summing all these probabilities to find the weighted time lag function (Ψ) and identifying the most probable points that correspond to the RTS levels [23]. Fig. 4(a) and (b) shows the W-TLP of DCR traces of a pixel selected from F2/A1 before and after irradiation, respectively. The plots indicate that, although this pixel exhibited no RTS behavior before irradiation, it displays multilevel RTS with five levels afterward. The edge detection method detailed in Section III-B, identifies three of these levels [Levels 1, 2, and 3 in Fig. 4(b)], whereas the W-TLP method discerns two additional levels at 1.196×10^5 Hz and 1.373×10^5 Hz.

With the aid of the real-time noise based edge-detection method (Section III-B), all five levels can be detected, and their values are close to the levels determined through W-TLP, as shown in Fig. 5. The figure includes the signal trace of the pixel at −20 °C after irradiation, with horizontal lines indicating the modified edge-detection levels (red solid) and W-TLP determined levels (black dashed-dotted). As illustrated in the figure, the two methods provide very similar results in terms of the number of RTS levels and their value, in particular at low temperatures, where Poisson noise is small, and the RTS transition rate is slow.

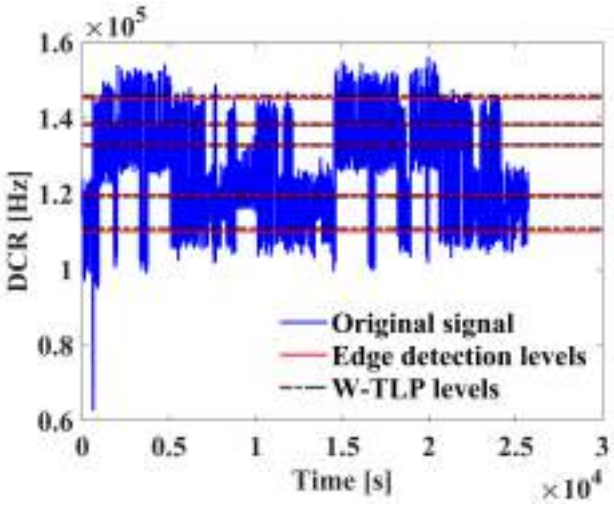

Fig. 5. DCR trace of pixel 11 × 22 from F2/A1 at an excess voltage V_{ex} = 2 V and −20 °C temperature after irradiation. Red solid and black dashed-dotted horizontal lines show the RTS levels identified by the real-time noise based edge detection and W-TLP methods, respectively.

At higher temperatures, especially after irradiation, where DCR switches rapidly between RTS levels and cannot be easily identified, W-TLP again becomes more reliable than the real-time noise based edge detection algorithm. This is illustrated in Fig. 6(a)–(d) by the DCR traces of a pixel selected from S2/A1 after irradiation. As shown in Fig. 6(a), at lower temperatures (10 °C and 20 °C), two distinct levels with large time constants are observable, and within the lower state, the time constant becomes smaller. However, as the temperature increases to 30 °C, the switching rate of RTS fluctuations increases, making it difficult for the real-time noise based edge detection method to identify RTS transitions correctly. This difficulty arises because detecting transitions with shorter time constants requires reducing the filter length, which, in turn, increases the risk of false detections [16]. This tradeoff is evident in Fig. 6(b), where the signal from the same pixel at 30 °C (within the time range of 1000–2000 s) shows both false level detection and inaccurate amplitude recognition. On the other hand, Fig. 6(c) shows the W-TLP plot of the RTS signal for the same pixel at the same temperature as in (b), where four distinct RTS levels can be identified. These identified levels are then overlaid on the original signal trace in Fig. 6(d), where a reliable identification of both the number of levels and their corresponding amplitudes is demonstrated.

Although W-TLP can accurately identify the number and values of RTS levels, it has a significant drawback: unlike the edge detection method, where RTS characteristic extraction, including time constants, is straightforward, this process becomes more complex with W-TLP, especially in the case of multi-level RTS. For example, with bi-level centers, only the ratio of time constants T_{up}/T_{down} can be determined by counting the number of occurrences in each level and calculating their ratio, but not the absolute values [24]. To find the absolute time constant values, additional equations obtained from histograms or power spectral density plots are required [24]. While this may not pose a problem for bi-level RTS, it becomes challenging for multi-level RTS.

TABLE II
NEUTRON FLUENCE AND CORRESPONDING DDD FOR EACH CHIP

Chip	Fluence (1 MeV neq cm^{-2})	DDD (TeV/g)
S2	3.90×10^{9}	4.35
F2	4.15×10^{10}	47

IV. RESULTS AND DISCUSSION

This section summarizes the results from the characterization of the tested CMOS SPAD arrays, also as a function of the temperature and the bias voltage. All the results shown in the following were obtained using the real-time noise based edge detection method.

A. Level Numbers and Defect Types

Fig. 7 illustrates the ratio of pixels featuring RTS fluctuations (RTS pixels) to the total pixel count in array A1 of chips (a) S2 and (b) F2, before and after irradiation. Note that in the figure, level 1 indicates a DCR with no RTS fluctuations, and the corresponding ratio represents the fraction of non-RTS pixels to the whole array.

In chip S2, the number of pixels featuring RTS fluctuations increases from 161 before irradiation to 600 afterward. Although bi-level RTS transitions remain dominant in S2, a notable rise in multi-level RTS pixels is observed post-irradiation. In chip F2, post-irradiation effects include a 28% increase in the proportion of RTS pixels, rising from 154 before irradiation to 801 afterward. Additionally, F2 exhibits the emergence of multilevel centers, leading to multi-level RTS fluctuations with up to nine levels. Despite the relatively small displacement damage dose (DDD) used in this study (reported in Table II), the presence of such a high number of levels is not surprising, as similar effects have been previously observed in CMOS image sensors (CIS) exposed to neutrons with a DDD of 39 TeV/g [25]. The more pronounced radiation-induced effects in F2 can be attributed to its exposure to a neutron fluence nearly an order of magnitude higher than that of S2.

To find out whether the multi-level RTS cases observed after irradiation arise from single multi-stable defects or from overlapping signals from multiple bi-level centers, a criterion outlined in [26] was applied to the four-level RTS pixels both in F2/A1 and S2/A1. This criterion, based on the hypothesis that simultaneous switching of two independent bi-level centers is highly improbable, suggests that transitions between the second and third levels, as well as between the first and fourth levels, should be rare [26]. Analysis revealed that, out of 262 four-level RTS pixels examined, only 12 were due to the superimposition of two bi-level centers. The remaining 250 pixels displayed behavior consistent with multilevel centers. The mean transition occurrence probabilities of these 250 pixels, detailed in Table III, further substantiate their

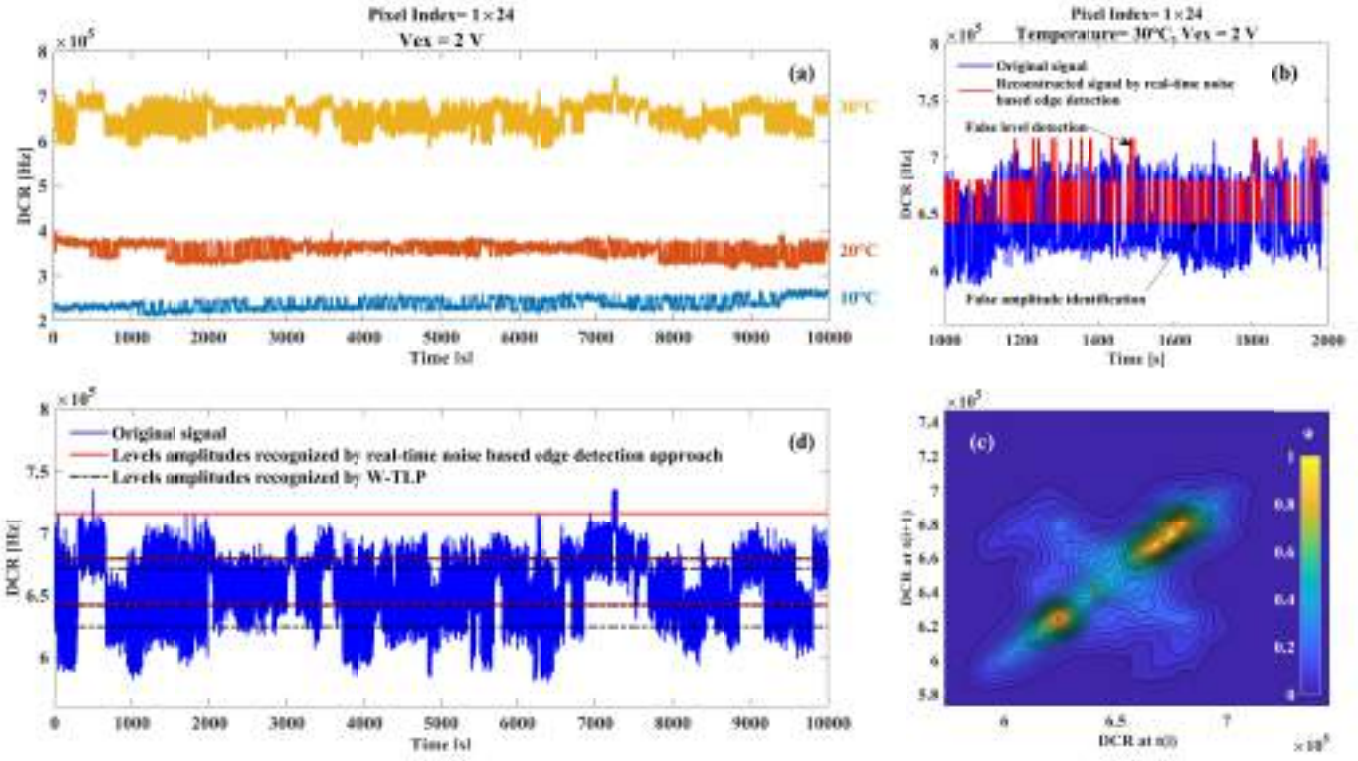

Fig. 6. (a) DCR traces of pixel 1 × 24 from S2/A1 at three temperatures of 10 °C, 20 °C, and 30 °C measured at an excess bias voltage V_{ex} = 2 V after irradiation. (b) Original DCR trace of the same pixel at 30 °C, overlaid with a reconstructed signal using a real-time noise based edge detection method, demonstrating reduced accuracy at higher temperatures. (c) W-TLP plot of the signal trace shown in (b). (d) Comparison between the number and amplitudes of levels detected by the improved edge detection algorithm and the W-TLP method.

TABLE III

MEAN RTS TRANSITION OCCURRENCE PROBABILITIES FOR PIXELS WITH FOUR-LEVEL RTS. IN EACH CELL, THE VALUE INDICATES THE PROBABILITY FOR DCR TO SWITCH FROM THE LEVEL INDICATED AT THE FAR LEFT OF THE ROW TO THE LEVEL INDICATED AT THE TOP OF THE COLUMN

	Level 1	Level 2	Level 3	Level 4
Level 1	0.0	19.7%	4.3%	1.7%
Level 2	19.8%	0.0	8.9%	4.2%
Level 3	4.2%	9%	0.0	11.2%
Level 4	1.7%	4.2%	11.1%	0.0

classification as multilevel centers, where transitions between adjacent levels (such as from level 2 to 3 and vice versa, or from 3 to 4 and vice versa) occur most often, a typical trait of multi-stable centers [26]. Additionally, for three-level RTS pixels, the inequality of transition amplitudes between levels 1–2 and levels 2–3 in many such pixels suggests that the RTS is caused by multi-stable defects rather than two similar bi-level defects; otherwise, the two amplitude values would be close to each other [26].

Fig. 8 displays the distribution of the average DCR for all pixels in array A1 of the two chips under test before irradiation, and after irradiation for RTS and non-RTS pixels. The histograms show a general increase in average DCR after exposure to irradiation. The similarity in the shape of the DCR distributions for RTS and non-RTS pixels suggests that RTS defects contribute to the DCR increase in a manner comparable to non-RTS centers. In other words, RTS defects do not exhibit a distinct average DCR signature that would differentiate them from non-RTS ones.

B. Temperature and Voltage Dependence

Fig. 9 shows DCR traces for a pixel belonging to F2/A1 at an excess voltage of 2 V and at various temperatures, after irradiation. Note that a logarithmic scale is used for the vertical axis. Before irradiation, the same pixel did not exhibit RTS at lower temperatures, and as the temperature increased, it displayed at most two-level RTS. A general trend, which was observed regardless of whether irradiation was applied, is that the transition amplitude increases with temperature, while the time constants decrease. Investigating the variations in the characteristics of RTS with temperature may yield insights into the defects responsible for RTS behavior. Before irradiation, 18 out of 24 pixels measured with a high-resolution setup exhibited no RTS at lower temperatures, and as the temperature increased, the maximum number of RTS levels they displayed was two. After irradiation, in addition to a faster switching rate, the number of levels also increases with temperature. As a result, starting from room temperature, the accuracy of the real-time noise based edge detection method decreases, making the correct detection of level numbers and values difficult. The increment in level numbers with temperature has been confirmed by inspection at lower temperatures,

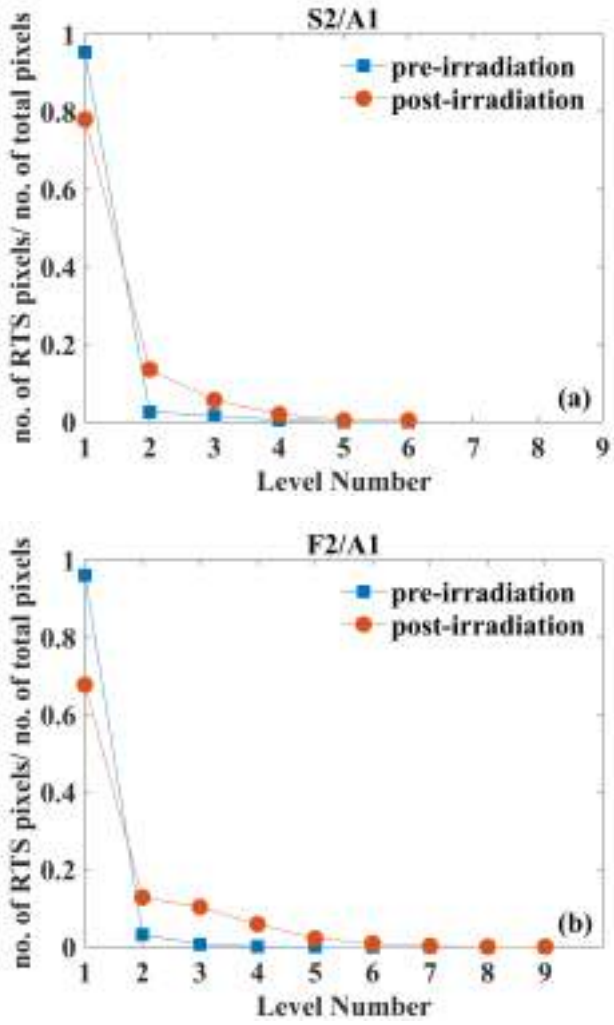

Fig. 7. Proportion of pixels showing RTS with a designated number of levels relative to the total pixel count in arrays A1, before and after irradiation, for chips (a) S2 and (b) F2.

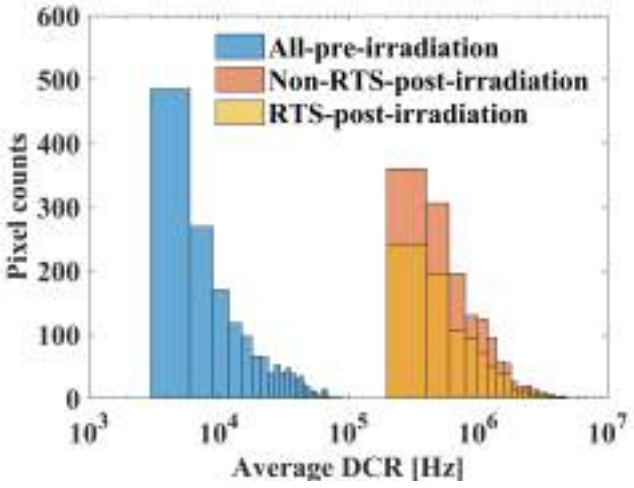

Fig. 8. Distribution of the average DCR for 4608 pixels before irradiation, 3124 non-RTS pixels, and 1484 RTS pixels after irradiation.

where accurate detection is possible. For instance, in the case of Fig. 9, the number of detected levels is 4, 6, and 8 at temperatures of −20 °C, −10 °C, and 0 °C, respectively. This behavior, already observed in the DCR of SPADs exposed to gamma rays, is ascribed to a decrease in time constants with temperature [11].

RTS has been proved to be a field-dependent phenomenon [15], [27]. Fig. 10 shows the DCR traces of two pixels (a) before irradiation and (b) after irradiation at various excess bias voltages. RTS amplitude is found to increase with the bias voltage. For instance, in Fig. 10(a), the RTS amplitude increases from 471 counts/s (cps) at V_{ex} = 1 V to 943 cps at V_{ex} = 2 V. Such an increase in amplitude can be attributed to both the higher avalanche probability [6] and also the contribution of electric field enhancement (EFE) effects [8]. However, the time constants of both levels remain virtually unchanged. In the case of Fig. 10(b), not only does the RTS amplitude increase, but the number of levels also increases from four to seven levels. Such behavior has been observed in other pixels and may be attributed to the fact that higher voltages can elevate the RTS amplitude above the Poisson noise, thereby making it detectable.

C. RTS Amplitude

The statistical distribution of RTS maximum transition amplitude (A_{max}) before and after irradiation are presented in Fig. 11. This A_{max} corresponds to the transition with the largest amplitude among all RTS transitions in a signal trace associated with each pixel. The graph clearly shows that the maximum amplitude increases post-irradiation. Unlike gamma-ray-induced RTS, which is caused by point defects in the SPAD active region and exhibits a Gaussian distribution for lower maximum amplitudes [11], neutron-induced RTS shows an almost exponential dependence across the entire range. Note that both the x- and y-axes in Fig. 11 are shown on a logarithmic scale. The difference in RTS amplitude histograms, despite displacement damage being the underlying mechanism for both types of radiation, may be attributed to the nature of the defects involved: point defects for gamma rays and clustered defects for neutrons. Protons, on the other hand, can generate a mixture of both point and clustered defects, and their RTS maximum transition amplitude distribution accordingly exhibits features of both Gaussian and exponential characteristics [11].

In the literature, it has been repeatedly observed that RTS maximum amplitude (A_{max}) and RTS amplitude (A_{RTS}) follow the Arrhenius law [8], [15], [25], [26]

$$A_{max}\ ,\ A_{RTS} \propto \exp\left(\frac{-E_a}{k_B T}\right) \tag{1}$$

where E_a is the activation energy that provides information about the dominating carrier generation mechanism for a specific level [25], k_B is the Boltzmann constant, and T is the temperature in Kelvin. As also mentioned in Section IV-B, the number of RTS levels increases with temperature after irradiation. Among all pixels measured using the high-resolution setup—except for two which showed bi-level RTS behavior at most temperatures—none were found to feature the same number of levels across various temperatures, thus making it impossible to determine activation energies

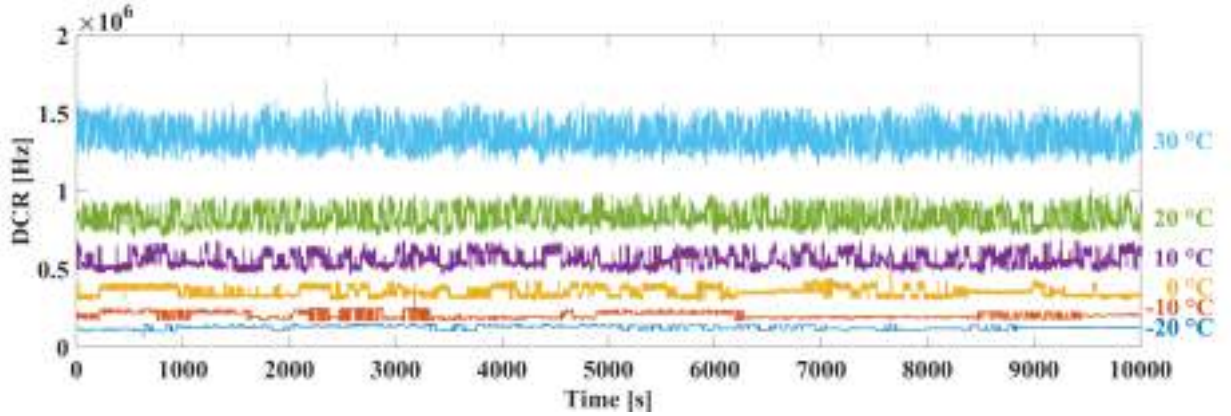

Fig. 9. DCR traces of pixel 11 × 22 from F2/A1 at an excess voltage V_{ex} = 2 V and various temperatures after irradiation with a fluence of 4.3×10^{10} 1 MeV neq cm^{-2}.

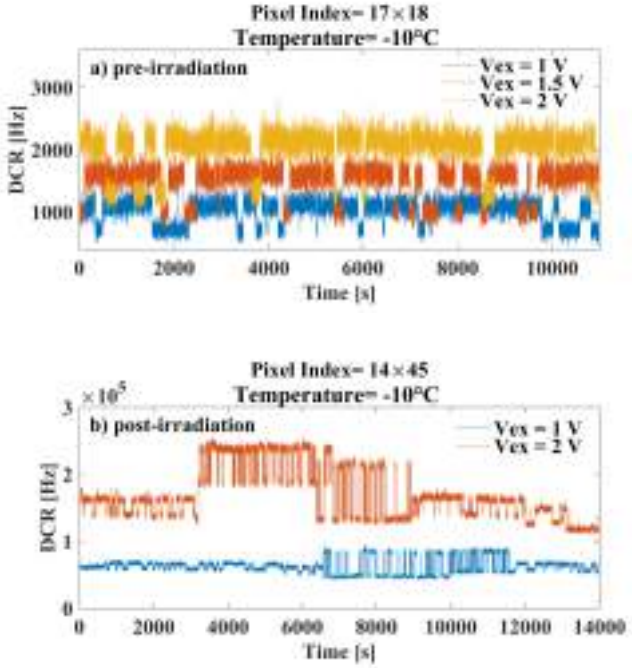

Fig. 10. DCR traces of (a) pixel 17 × 18 at three different V_{ex}, 1, 1.5, and 2 V, before irradiation and (b) pixel 14 × 45 at two V_{ex} of 1 and 2 V after irradiation both from F2/A1.

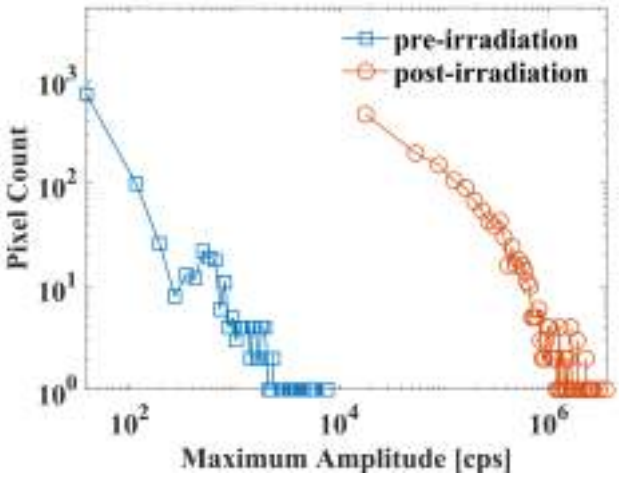

Fig. 11. Maximum amplitude (A_{max}) distribution before and after irradiation for array A1 in both chips. The distributions were obtained at a temperature of 25 °C and an excess voltage of V_{ex} = 1.5 V.

associated with each transition amplitude for pixels exhibiting multi-level RTS behavior. However, it is still feasible to obtain E_a for the maximum RTS amplitude before and after irradiation and conduct a comparison. Fig. 12 shows the Arrhenius plot for the maximum transition amplitude of two representative pixels (a) before and (b) after irradiation. The calculated activation energy of 0.33 eV before irradiation suggests that for the upper level, DCR generation is enhanced by the electric field [25], as stated previously. The nearly identical E_a after irradiation indicates the same carrier generation mechanism. Among the other high-resolution measured pixels, 23 were found after irradiation, whose maximum amplitude mostly follows the Arrhenius law with a single trend across the entire temperature range, yielding an average activation energy of 0.29 eV.

D. Pulsewidth and Time Constants

The pulsewidth distribution of each level is expected to follow an exponential distribution [8], [15], [26]. This has also been verified in this study, as shown in Fig. 13. In this figure, the pulsewidth distribution of each level of a four-level RTS is plotted, accompanied by a fitting exponential curve. The extracted average times are reported within each figure, indicating that levels two and four are more stable than the other two levels

$$\tau \propto \exp\left(\frac{E_{ab}}{k_{BT}}\right). \tag{2}$$

Fig. 14 shows the time constant distribution of RTS pixels from both F2/A1 and S2/A1 characterized with the high resolution setup at two different temperatures (−20 °C and 0 °C) after neutron irradiation. As previously mentioned, the switching rate of RTS transitions increases with temperature,

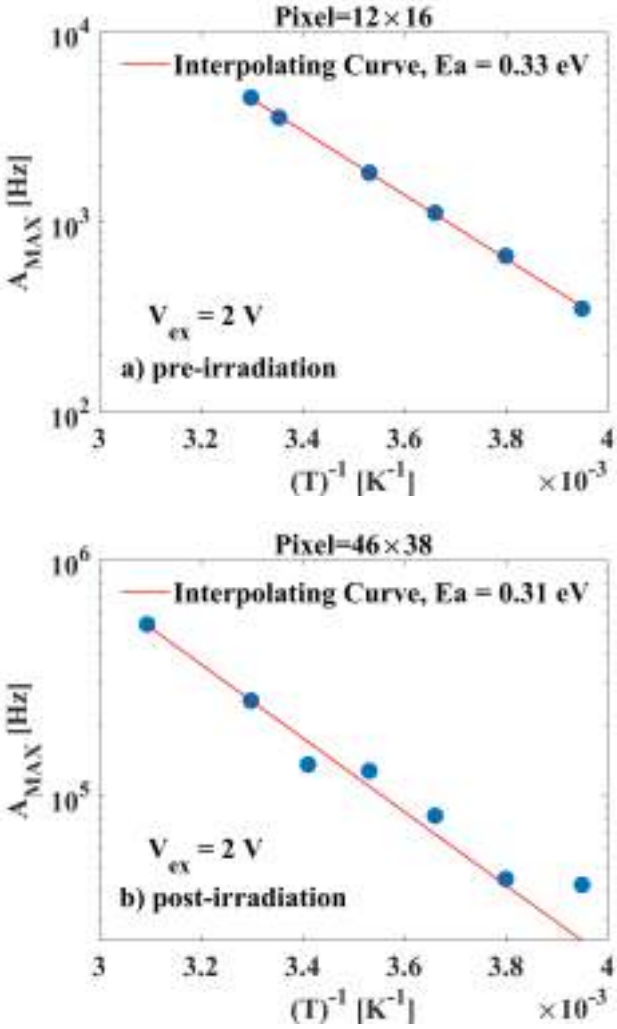

Fig. 12. Arrhenius plots for maximum transition amplitude ($A_{\max}$) in pixel 12 × 16 from F2/A1 (a) before irradiation, showing a single trend with $E_a \simeq 0.33$ eV, and in pixel 46 × 38 from F2/A1 and (b) after irradiation with $E_a \simeq 0.31$ eV.

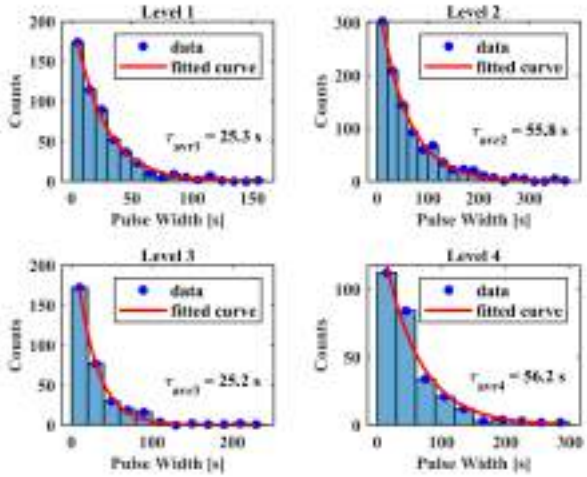

Fig. 13. Pulsewidth distribution for each level of a four-level RTS measured in the DCR trace of pixel 12 × 16 from F2/A1 at a temperature of 40 °C and an excess voltage of 2 V post-irradiation. The distributions are shown for ascending RTS levels. The blue dots represent the midpoints of the histogram bins, and the red exponential line is the curve fitting to these bin centers. The average time (τ_{avr}) values are reported within each figure.

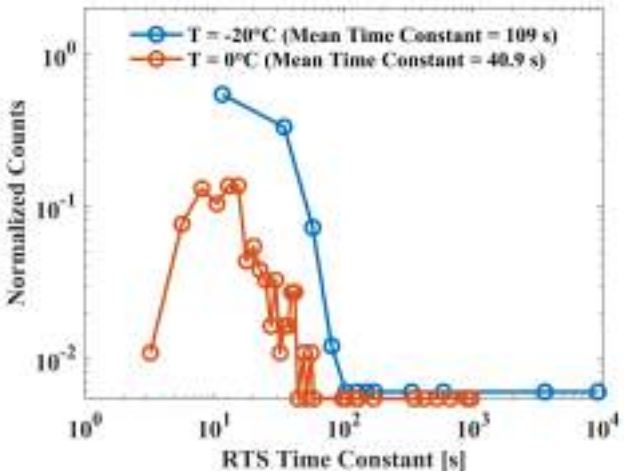

Fig. 14. Normalized time constant distributions of RTS pixels from both F2/A1 and S2/A1 after exposure to neutrons at temperatures of −20 °C (blue curve) and 0 °C (orange curve).

causing the distribution to shift toward lower time constants. Accordingly, the mean time constant decreases from 109 s at −20 °C to 40.9 s at 0 °C. These results can be compared to those from distributions reported in the literature [11] for SPADs exposed to γ-rays (DDD = 61 Tev/g) and protons (DDD = 396 TeV/g) at 25 °C, featuring mean values of 317 and 219.9 s, respectively. The comparison points to a significantly faster RTS noise in neutron irradiated SPADs than in the case of γ-rays and proton irradiated devices, even if measurements are taken at a lower temperature than in [11]. Moreover, the peak around 300 s observed in γ-rays and proton-induced RTS time constant distributions, which likely arise from point defects, is not present in Fig. 14. These observations may indicate that RTS in neutron-irradiated devices primarily originates from defect clusters rather than point defects and that clusters tend to generate faster-switching RTS events.

The extracted activation energy (E_{ab}) could provide insights into the energy barrier that an RTS defect needs to overcome to reconfigure from one stable state to another [10]. However, as previously mentioned for RTS amplitudes, after irradiation, the observed RTS is highly complex, and it is very difficult to find pixels in this study that display the same number of levels at various temperatures to extract reliable transition time constants. To study neutron-induced RTS defect types in our SPADs, other techniques such as high-temperature isochronal annealing could be employed [11]. For two pixels after irradiation, which predominantly exhibit two-level RTS across the temperature range, Arrhenius plots show a saturation of the time constants at low temperatures, as demonstrated for one of them in Fig. 15(a). Although corresponding DCR traces of the same pixel shown in Fig. 15(b), especially at 0 °C and 10 °C, may appear to suggest more than two levels, the real-time noise based edge-detection algorithm was specifically tuned to capture only the largest amplitude RTS transitions,

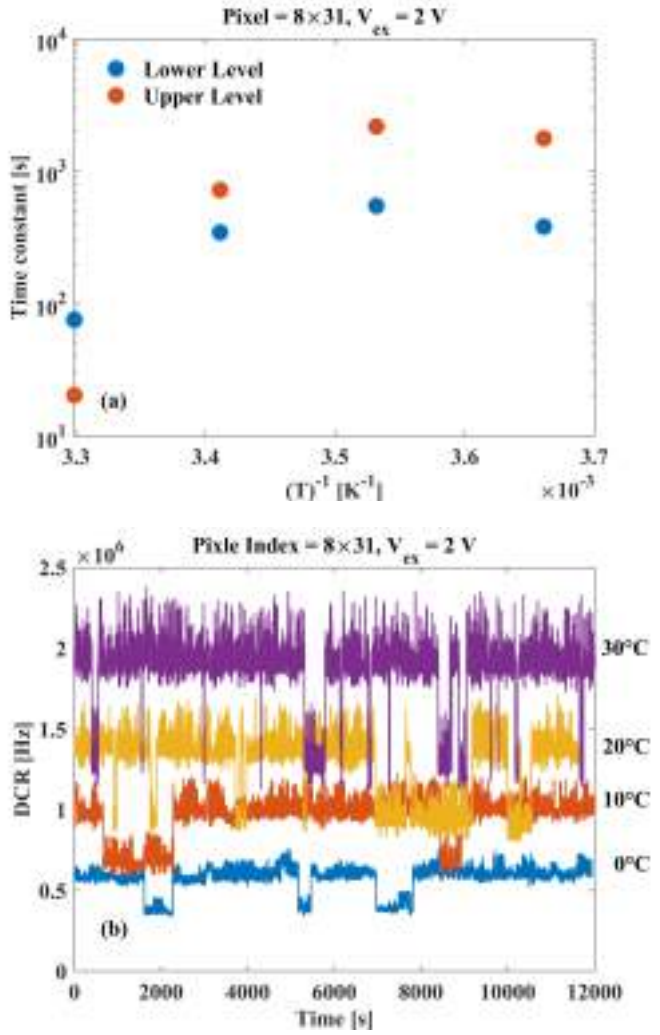

Fig. 15. (a) Lower- and upper-level time constants Arrhenius plots of a semi-bi-level RTS pixel from chip S2/A1 after irradiation, at an excess voltage of 2 V. (b) Corresponding DCR traces at the respective temperatures.

deliberately filtering out smaller fluctuations. This result has not been previously observed in the literature and warrants further investigation. Additionally, given the low number of such pixels, further statistical data is needed to confirm this finding.

V. Conclusion

In this study, various RTS analysis tools from the literature were compared to characterize neutron-induced RTS in two identical SPAD arrays fabricated in a 150-nm CMOS technology and exposed to fluences of 3.90×10^9 and 4.15×10^{10} 1 MeV neq cm^{-2}. Among these techniques, the real-time noise based edge detection approach proved to be accurate at lower temperatures and effective for RTS automatic feature extraction, whereas the W-TLP showed reliability at both low and high temperatures, albeit with more difficulty in feature extraction, in particular from the standpoint of time constants.

The results obtained using the improved edge detection approach demonstrated that neutron irradiation can increase the occurrence of RTS fluctuations in CMOS SPADs, as evidenced by an increase in the RTS pixel fraction of 19% in S2 and 28% in F2. Also, the number of RTS levels increases after irradiation, reaching a maximum of nine levels, even at the relatively low DDDs used in this research. Further analysis revealed that this increase in complexity is primarily due to the formation of multi-level defects rather than the superposition of multiple bi-level defects. A comparison of maximum amplitude distributions before and after irradiation revealed an increase in RTS amplitude due to radiation exposure.

The study of RTS behavior as a function of temperature and voltage provided limited insights into defect identification. Therefore, further research using high-temperature isochronal annealing may be beneficial for identifying defect types more accurately. Moreover, comparisons with SPADs irradiated by γ-rays and protons suggested that neutron-induced RTS is significantly faster than that induced by γ-rays, likely due to the formation of cluster defects. Therefore, tests with high-energy photons (e.g., gamma rays from ^{60}Co) on the same samples may help distinguish the effects of point defects from those of cluster defects induced by neutrons.

Acknowledgment

The authors thank Marco Musacci, who designed the chip characterized in this work.

References

[1] S. Zhuo et al., "Solid-state dToF LiDAR system using an eight-channel addressable, 20-W/Ch transmitter, and a 128 × 128 SPAD receiver with SNR-based pixel binning and resolution upscaling," *IEEE J. Solid-State Circuits*, vol. 58, no. 3, pp. 757–770, Mar. 2023, doi: 10.1109/JSSC.2022.3227078.

[2] L. H. C. Braga et al., "A fully digital 8 × 16 SiPM array for PET applications with per-pixel TDCs and real-time energy output," *IEEE J. Solid-State Circuits*, vol. 49, no. 1, pp. 301–314, Jan. 2014, doi: 10.1109/JSSC.2013.2284351.

[3] Y. Xu, P. Xiang, and X. Xie, "Comprehensive understanding of dark count mechanisms of single-photon avalanche diodes fabricated in deep sub-micron CMOS technologies," *Solid-State Electron.*, vol. 129, pp. 168–174, Mar. 2017, doi: 10.1016/j.sse.2016.11.009.

[4] M. A. Karami, L. Carrara, C. Niclass, M. Fishburn, and E. Charbon, "RTS noise characterization in single-photon avalanche diodes," *IEEE Electron Device Lett.*, vol. 31, no. 7, pp. 692–694, Jul. 2010, doi: 10.1109/LED.2010.2047234.

[5] H. Xu, L. Pancheri, G.-F.-D. Betta, and D. Stoppa, "Design and characterization of a p$^+$/n-well SPAD array in 150nm CMOS process," *Opt. Exp.*, vol. 25, no. 11, pp. 12765–12778, May 2017, doi: 10.1364/oe.25.012765.

[6] L. Ratti et al., "Cross-talk and RTS noise characterization of 1-and 2-tier CMOS SPADs in a 150 nm process," in *Proc. IEEE Nucl. Sci. Symp. Med. Imag. Conf.*, Piscataway, NJ, USA, Apr. 2021, pp. 225–228, doi: 10.1109/NSS/MIC44867.2021.9875825.

[7] G. Torilla et al., "DCR and crosstalk characterization of a bi-layered 24 × 72 CMOS SPAD array for charged particle detection," *Nucl. Instrum. Methods Phys. Res. A, Accel. Spectrom. Detect. Assoc. Equip.*, vol. 1046, Jan. 2023, Art. no. 167693, doi: 10.1016/j.nima.2022.167693.

[8] F. Di Capua et al., "Random telegraph signal in proton irradiated single-photon avalanche diodes," *IEEE Trans. Nucl. Sci.*, vol. 65, no. 8, pp. 1654–1660, Aug. 2018, doi: 10.1109/TNS.2018.2814823.

[9] M. Campajola, F. Di Capua, D. Fiore, C. Nappi, E. Sarnelli, and L. Gasperini, "Radiation effects on single-photon avalanche diodes manufactured in deep submicron CMOS technology," *J. Phys., Conf. Ser.*, vol. 1226, no. 1, May 2019, Art. no. 012007, doi: 10.1088/1742-6596/1226/1/012007.

[10] F. D. Capua, M. Campajola, D. Fiore, L. Gasparini, E. Sarnelli, and A. Aloisio, "Investigation of random telegraph signal in two junction layouts of proton irradiated CMOS SPADs," *Sci. Rep.*, vol. 11, no. 1, Apr. 2021, Art. no. 8580, doi: 10.1038/s41598-021-87962-w.

[11] A. Jouni et al., "Effects of X-ray and γ-Ray irradiations on 2-D-Planar and 3-D-stacked CMOS SPADs," *IEEE Trans. Nucl. Sci.*, vol. 71, no. 8, pp. 1753–1765, Aug. 2024, doi: 10.1109/TNS.2024.3406511.

[12] A. Jay et al., "Simulation of single-particle displacement damage in silicon—Part III: First principle characterization of defect properties," *IEEE Trans. Nucl. Sci.*, vol. 65, no. 2, pp. 724–731, Feb. 2018, doi: 10.1109/TNS.2018.2790843.

[13] A. Jay et al., "Simulation of single particle displacement damage in silicon—Part II: Generation and long-time relaxation of damage structure," *IEEE Trans. Nucl. Sci.*, vol. 64, no. 1, pp. 141–148, Jan. 2017, doi: 10.1109/TNS.2016.2628089.

[14] I. H. Hopkins and G. R. Hopkinson, "Random telegraph signals from proton-irradiated CCDs," *IEEE Trans. Nucl. Sci.*, vol. 40, no. 6, pp. 1567–1574, Dec. 1993, doi: 10.1109/23.273552.

[15] D. Fiore, "Random telegraph signal in CMOS single photon avalanche diodes," Ph.D. Dissertation, Dept. of Engineering for the Environment and the Territory and Chemical Engineering, Calabria Univ., Arcavacata, Italy, 2019, doi: 10.13126/unical.it/dottorati/1788.

[16] V. Goiffon, G. R. Hopkinson, P. Magnan, F. Bernard, G. Rolland, and O. Saint-Pe, "Multilevel RTS in proton irradiated CMOS image sensors manufactured in a deep submicron technology," *IEEE Trans. Nucl. Sci.*, vol. 56, no. 4, pp. 2132–2141, Aug. 2009, doi: 10.1109/TNS.2009.2014759.

[17] D. J. Oh, S. K. Kwon, H. S. Song, S. Y. Kim, G. W. Lee, and H. D. Lee, "Methodology for extracting trap depth using statistical RTS noise data of capture and emission time constant," *J. Semicond. Technol. Sci.*, vol. 17, no. 2, pp. 252–259, Apr. 2017, doi: 10.5573/JSTS.2017.17.2.252.

[18] F. Shojaei et al., "Bulk damage effects in neutron irradiated single- and dual-layer 150-nm CMOS SPADs," *IEEE Trans. Nucl. Sci.*, vol. 72, no. 3, pp. 908–918, Mar. 2025, doi: 10.1109/TNS.2025.3530240.

[19] F. Pino et al., "Characterization of a fast neutron irradiation facility using a stilbene scintillation detector," *Nucl. Technol.*, vol. 210, no. 10, pp. 1975–1984, Mar. 2024, doi: 10.1080/00295450.2024.2304993.

[20] L. Ratti et al., "Layered CMOS SPADs for low noise detection of charged particles," *Frontiers Phys.*, vol. 8, Jan. 2021, Art. no. 607319, doi: 10.3389/fphy.2020.607319.

[21] L. Pancheri and D. Stoppa, "Low-noise single photon avalanche diodes in 0.15 μm CMOS technology," in *Proc. Eur. Solid-State Device Res. Conf. (ESSDERC)*, Helsinki, Finland, Sep. 2011, pp. 179–182, doi: 10.1109/ESSDERC.2011.6044205.

[22] R. Zheng et al., "A real-time auto-detection method for random telegraph signal (RTS) noise detection in CMOS active pixel sensors," *J. Instrum.*, vol. 10, no. 7, Jul. 2015, Art. no. C07013, doi: 10.1088/1748-0221/10/07/c07013.

[23] J. Martin-Martinez, J. Diaz, R. Rodriguez, M. Nafria, and X. Aymerich, "New weighted time lag method for the analysis of random telegraph signals," *IEEE Electron Device Lett.*, vol. 35, no. 4, pp. 479–481, Apr. 2014, doi: 10.1109/LED.2014.2304673.

[24] E. Simoen, W. Fang, M. Aoulaiche, J. Luo, C. Zhao, and C. Claeys, "Random telegraph noise: The key to single defect studies in nano-devices," *Thin Solid Films*, vol. 613, pp. 2–5, Aug. 2016, doi: 10.1016/j.tsf.2015.08.037.

[25] C. Virmontois et al., "Total ionizing dose versus displacement damage dose induced dark current random telegraph signals in CMOS image sensors," *IEEE Trans. Nucl. Sci.*, vol. 58, no. 6, pp. 3085–3094, Dec. 2011, doi: 10.1109/TNS.2011.2171005.

[26] C. Durnez, V. Goiffon, C. Virmontois, J.-M. Belloir, P. Magnan, and L. Rubaldo, "In-depth analysis on radiation induced multi-level dark current random telegraph signal in silicon solid state image sensors," *IEEE Trans. Nucl. Sci.*, vol. 64, no. 1, pp. 19–26, Jan. 2017, doi: 10.1109/TNS.2016.2633333.

[27] M. A. Karami, A. Pil-Ali, and M. R. Safaee, "Multistable defect characterization in proton irradiated single-photon avalanche diodes," *Opt. Quantum Electron.*, vol. 47, no. 7, pp. 2155–2160, Dec. 2014, doi: 10.1007/s11082-014-0089-7.